Atmos. Meas. Tech. Discuss., 7, 4909–4947, 2014
www.atmos-meas-tech-discuss.net/7/4909/2014/
doi:10.5194/amtd-7-4909-2014
© Author(s) 2014. CC Attribution 3.0 License.

Atmospheric Measurement Techniques Discussions
Open Access

This discussion paper is/has been under review for the journal Atmospheric Measurement Techniques (AMT). Please refer to the corresponding final paper in AMT if available.

FAME-C: cloud property retrieval using synergistic AATSR and MERIS observations

C. K. Carbajal Henken, R. Lindstrot, R. Preusker, and J. Fischer

Institute for Space Sciences, Freie Universität Berlin (FUB), Berlin, Germany

Received: 29 April 2014 – Accepted: 1 May 2014 – Published: 19 May 2014

Correspondence to: C. K. Carbajal Henken (cintia.carbajal@wew.fu-berlin.de)

Published by Copernicus Publications on behalf of the European Geosciences Union.

Abstract

A newly developed daytime cloud property retrieval algorithm FAME-C (Freie Universität Berlin AATSR MERIS Cloud) is presented. Synergistic observations from AATSR and MERIS, both mounted on the polar orbiting satellite ENVISAT, are used for cloud screening. For cloudy pixels two main steps are carried out in a sequential form. First, a micro-physical cloud property retrieval is performed using an AATSR near-infrared and visible channel. Cloud phase, cloud optical thickness, and effective radius are retrieved, and subsequently cloud water path is computed. Second, two independent cloud top height products are retrieved. For cloud top temperature AATSR brightness temperatures are used, while for cloud top pressure the MERIS oxygen-A absorption channel is used. Results from the micro-physical retrieval serve as input for the two cloud top height retrievals. Introduced are the AATSR and MERIS forward models and auxiliary data needed in FAME-C. Also, the optimal estimation method with uncertainty estimates, which also provides for uncertainty estimated of the retrieved property on a pixel-basis, is presented. Within the frame of the ESA Climate Change Initiative project first global cloud property retrievals have been conducted for the years 2007–2009. For this time period verification efforts are presented comparing FAME-C cloud micro-physical properties to MODIS-TERRA derived cloud micro-physical properties for four selected regions on the globe. The results show reasonable accuracies between the cloud micro-physical retrievals. Biases are generally smallest for marine stratocumulus clouds; −0.28, 0.41 µm and $-0.18\,\mathrm{g\,m^{-2}}$ for cloud optical thickness, effective radius and cloud water path, respectively. This is also true for the root mean square error. Also, both cloud top height products are compared to cloud top heights derived from ground-based cloud radars located at several ARM sites. FAME-C mostly shows an underestimation of cloud top heights when compared to radar observations, which is partly attributed to the difficulty of accurate cloud property retrievals for optically thin clouds and multi-layer clouds. The bias is smallest, −0.9 km, for AATSR derived cloud top heights for single-layer clouds.

AMTD
7, 4909–4947, 2014

1 Introduction

In the Earth's present climate system clouds play a key role through their strong interaction with solar radiation and thermal radiation emitted by the Earth's surface and atmosphere as well as their dominant role in the hydrological cycle. On average about 70 % of the Earth's surface is covered by clouds and their temporal and spatial variability is high. Climate models are used to improve our understanding of regional and global climate and to project future climate changes. However, low confidence is given to the representation and quantification of cloud processes in these models, especially in combination with aerosol processes. Cloud adjustments due to aerosols still contribute the largest uncertainty to the total radiative forcing estimate (IPCC, 2013).

Accurate observations of cloud properties on a global scale are needed for climate model development and evaluation as well as for climate research. Satellite observations provide these global and long-term cloud observations. From observations in the shortwave and longwave part of the electromagnetic spectrum cloud micro-physical properties such as cloud thermodynamic phase, cloud optical thickness and effective radius, which describes the cloud droplet size distribution, as well as cloud macro-physical properties, such as cloud amount and cloud top height, can be retrieved.

A number of these types of cloud property retrievals and their accompanying global, long-term cloud data sets exist for a range of multi-spectral passive imagers on both polar-orbiting and geostationary satellites. Several of these data sets are included in the GEWEX Assesment of Global Cloud Datasets from Satellites (Stubenrauch et al., 2012). The Ojective of this assessment is to evaluate their overall quality. Participating cloud data sets include the International Satellite Cloud Climatology Project (ISCCP, 2013) based on observations from imagers on a set of satellites, the Pathfinder Atmospheres Extended (PATMOS-X, 2013) based on observations from the Advanced Very High Resolution Radiometer (AVHRR) instrument on NOAA and EUMETSAT polar-orbiting satellites, and cloud products from the MODIS Science Team (NASA, 2013b) and MODIS CERES Science Team (NASA, 2013a), using MODIS observations from

AMTD
7, 4909–4947, 2014

the polar-orbiting satellites AQUA and TERRA. Inter-comparisons were performed on monthly mean, gridded cloud data sets. Results show that differences in average cloud properties mainly arise due to differences in the instrument capability to detect thin cirrus clouds, especially over low-level water clouds.

To assess the quality of retrieved cloud properties due to algorithm design itself, i.e. not accounting for instrument design, the Cloud Retrieval Evaluation Workshop (CREW) was initiated by EUMETSAT (Roebeling et al., 2013). Level-2 cloud products derived from a set of well-established cloud property algorithms have been collected and inter-compared for pre-defined days against observations from the active instruments CALIOP on CALIPSO, CPR on CloudSat and AMSR on AMSU, all part of the the A-train constellation. Participating cloud property algorithms include the Clouds and Earth's Radiant Energy System (CERES) algorithm (Minnis et al., 2011), PATMOS-X including the Daytime Cloud Optical and Micro-physical Properties (DCOMP) algorithm (Walther and Heidinger, 2012), the Cloud Physical Properties (CPP) algorithm (Roebeling et al., 2006), and the Oxford-RAL Retrieval of Aerosol and Cloud (ORAC) algorithm (Poulsen et al., 2011). These kind of studies can reveal strengths and weaknesses of different methods of cloud property retrievals and has shown that large differences can already arise due to different cloud detection methods. This will in turn also affect temporal and spatial averages of cloud properties for climate studies.

In the frame of the ESA Climate Change Initiative (CCI) Cloud project (ESA, 2013c) a 10 year daytime cloud climatology of synergistic AATSR (Advanced Along-Track Scanning Radiometer) and MERIS (Medium Resolution Imaging Spectrometer), both flying on the ENVISAT satellite, cloud observations is to be produced. The ultimate objective of the project is to provide long-term coherent cloud property data sets for climate research, taking advantage of the synergy of different earth observation missions. The FAME-C (Freie Universitäet Berlin AATSR MERIS Cloud) algorithm uses optimal estimation to retrieve a set of daytime cloud properties and their uncertainties on a pixel basis. Originally, MERIS and AATSR were not designed for cloud observations, but together they provide a useful set of channels in the visible, near-infrared

AMTD
7, 4909–4947, 2014

and infrared wavelengths for cloud property retrieval. Furthermore, two independent cloud height products are retrieved, using once AATSR brightness temperatures from two infrared channels and once the MERIS oxygen-A absorption channel. Follow-up instruments SLSTR (Sea and Land Surface Temperature Radiometer) and OLCI (Ocean Land Colour Instrument) onboard Sentinel-3 (ESA, 2013e), expected to be launched by mid 2015, will have very similar channel settings, making the FAME-C algorithm applicable for their observations as well.

This paper is intended to serve as a reference to the FAME-C algorithm. The structure of the paper is as follows. First, the AATSR and MERIS observations are introduced and pre-processing is shortly explained in Sect. 2. Section 3 presents the forward models used in the cloud-micro-physical retrieval, and in both cloud top temperature and pressure retrievals. Also, a short note on auxiliary data is given. Next, Sect. 4 presents an overview of the retrieval scheme, treating the applied inversion technique and listing uncertainty estimates. Section 5 shows verification results of the comparison of FAME-C level-2 cloud properties with MODIS-TERRA micro-physical cloud properties and cloud top heights derived from ground-based radar observations. Last, a summary and discussion is given.

2 Observation data and pre-processing

2.1 Instruments

AATSR and MERIS are both imaging multi-spectral radiometers mounted on the polar orbiting satellite ENVISAT, which was launched in March 2002 and was in operational use until April 2012, providing a 10 years measurement data set. ENVISAT flies in a sun-synchronous polar orbit around the earth at a mean altitude of 800 km and and a 98.5° inclination. It has a repeat cycle of 35 days and the mean local solar time at descending node is 10.00 a.m. The MERIS instrument has fifteen spectral channels, which are programmable in position and width within the visible spectral range (390 to

AMTD
7, 4909–4947, 2014

1040 nm), and scans the earth with a push-broom method. It has a horizontal resolution of just over 1 km at the sub-satellite point and its field of view, resulting in a swath width of 1150 km, is covered using five identical optical cameras. AATSR has spectral channels in the visible range as well as in the near-infrared and infrared range of the spectrum (channels at 0.6, 0.8, 1.6, 3.7, 10.8, 12 µm). It has a horizontal resolution of 1 km at sub-satellite point and a swath width of about 500 km. Due to its conical scanning method it has a dual-view of the earth surface for all spectral channels. More details on both instruments can be found at ESA (2013d).

2.2 Collocation and cloud screening

Cloud property retrievals are performed for pixels identified as cloudy by a synergistic cloud mask, which is produced using the cloud screening module in the BEAM toolbox (ESA, 2013a). First, the AATSR observations are collocated with MERIS observations on the MERIS grid (reduced resolution mode; 1200 m × 1000 m) using a nearest neighbour technique. This grid has been chosen due to MERIS's better geo-location. Then, a cloud screening is performed combining a set of neural networks optimized for different cloudy situations and using all AATSR and MERIS channels. Finally, the produced synergy product contains all AATSR and MERIS channels as well as the newly produced cloud flag and cloud abundance parameters. It should be noted that the synergy product contains all pixels within the AATSR swath, meaning that the end product has a swath width of 500 km. Technical details on the collocation and cloud screening method can be found in Gómez-Chova et al. (2008) and Gómez-Chova et al. (2010).

2.3 Drift and straylight correction

An improved long-term drift correction is applied on the AATSR reflectances for the visible and near-infrared channels from the third reprocessing as described in Smith et al. (2008). Also for MERIS the third reprocessing has been used (ESA, 2011). Furthermore, an empirical straylight correction has been applied on the reflectance of the

AMTD
7, 4909–4947, 2014

MERIS oxygen-A absorption channel, which depends on the center wavelength of the oxygen-A absorption channel (Lindstrot et al., 2010).

3 Forward model

3.1 Micro-physical cloud properties

The retrieval of the cloud micro-physical properties cloud optical thickness (COT, τ) and effective radius (REF, r_{eff}) for water and ice clouds, and subsequently also cloud water path (CWP), is based on the DCOMP algorithm and largely follows the approach as described in Walther and Heidinger (2012). The COT-REF pair is retrieved using simultaneous measurements of the AATSR 0.6 µm and 1.6 µm channels. It is based on the assumption that the reflectance in the visible (VIS) mainly depends on COT due to conservative scattering, while the reflectance in the near-infrared (NIR) mainly depends on the cloud droplet size distribution due to weak absorption. This method is based on work by Nakajima and King (1990) and since has been used in a number of cloud property retrievals (e.g. Nakajima and Nakajma, 1995; Roebeling et al., 2006; Walther and Heidinger, 2012).

Look-Up-Tables (LUTs) for both water and ice clouds consisting of cloud reflectances have been created with simulations from the radiative transfer model Matrix Operator Model (MOMO). MOMO has been developed at the Freie Universität Berlin (Fell and Fischer, 2001; Hollstein and Fischer, 2012) and allows for simulations of radiative transfer in a plane-parallel homogeneous scattering medium with any vertical resolution. The cloud reflectance $R_{\text{c},\lambda}$, at wavelength λ (wavelength dependency will not be used in the text from now on), is given by:

$$R_{\text{c},\lambda} = \frac{\pi \times L_{\lambda}(\theta_0, \theta, \phi, \tau, r_{\text{eff}})}{\cos(\theta_0) \times F_{0,\lambda}(\theta_0)}, \quad (1)$$

AMTD
7, 4909–4947, 2014

where L is the reflected radiance by the cloud and F_0 is the incoming solar irradiance at the top of the atmosphere. The radiance L is a function of solar zenith angle θ_0, viewing zenith angle θ, and relative azimuth difference ϕ, as well as cloud optical thickness and effective radius. The simulations have been performed assuming a homogeneous cloud and no contribution from the atmosphere as well as the surface, i.e. no gaseous absorption, Rayleigh scattering, aerosol extinction, and zero surface albedo. The reflectance at the cloud top R_{toc}, when including a Lambertian reflecting surface, is computed as follows:

$$R_{\mathrm{toc},\lambda} = R_{\mathrm{c},\lambda} + \frac{\alpha_\lambda \times t_{\mathrm{c},\lambda}(\theta_0,\tau,r_{\mathrm{eff}}) \times t_{\mathrm{c},\lambda}(\theta,\tau,r_{\mathrm{eff}})}{1-\alpha_\lambda \times S_\lambda(\tau,r_{\mathrm{eff}})}, \quad (2)$$

where α is the surface albedo, $t_{\mathrm{c}}(\theta_0)$ and $t_{\mathrm{c}}(\theta)$ are the cloud transmittance in the downward and upward directions, respectively, and S is the spherical albedo.

To compare the measurements, which are reflectances at the top of atmosphere R_{toa}, to the forward model results, which are reflectances observed at cloud top, the measured reflectances are corrected for atmospheric extinction of radiation due to gaseous absorption both above and below the cloud, and Rayleigh scattering only considered above the cloud. Other sources of extinction, e.g. aerosols, are not considered. The top of cloud reflectance R_{toc} is computed from the measured top-of-atmosphere reflectance R_{toa} as follows:

$$R_{\mathrm{toc},\lambda} = \frac{R_{\mathrm{toa},\lambda} - R_{\mathrm{RS},\lambda}(\theta_0,\theta,\phi,\tau,r_{\mathrm{eff}},p_{\mathrm{c}})}{t_{\mathrm{a},\lambda}(\theta,\theta_0)}, \quad (3)$$

where R_{RS} is the amount of extinction due to Rayleigh scattering, and t_{a} is the two-way atmospheric transmittance above the cloud. The Rayleigh scattering correction is based on Wang and King (1997) and is only performed in the VIS channel. Next to the viewing geometry it depends on cloud albedo α_{c}, which in turn depends on COT and REF, and Rayleigh optical thickness from cloud top to top of atmosphere, τ_{r}.

AMTD
7, 4909–4947, 2014

The Rayleigh optical thickness is determined assuming a total column Rayleigh optical thickness of 0.044 (at surface pressure 1013 hPa) and scaling it by an estimated cloud top pressure p_c. Above the cloud the transmittance of the atmosphere is determined considering absorption by water vapor (total column water vapor above cloud) and ozone (total ozone in dobson units) in the VIS channel and only absorption by water vapor in the NIR channel. A quadratic relationship, and its accompanying coefficients, between the total amount of water vapor and ozone above cloud and the transmittance, depending on airmass, have been determined using a number of MODTRAN simulations. More information can be found in Walther and Heidinger (2012). The atmospheric correction coefficients for the AATSR channels are listed in Table 1. Below the cloud diffuse scattering is assumed, therefore setting the airmass to 2. The surface albedo α is then adjusted to a so called virtual surface albedo α_v by multiplying it with the atmospheric transmittance below the cloud. The altitude of the cloud is roughly estimated using the AATSR 10.8 µm brightness temperature. The full forward model looks as follows:

$$R_{\mathrm{toc},\lambda} = R_{\mathrm{c},\lambda} + \frac{\alpha_{\mathrm{v},\lambda} \times t_{\mathrm{c},\lambda}(\theta_0, \tau, r_{\mathrm{eff}}) \times t_{\mathrm{c},\lambda}(\theta, \tau, r_{\mathrm{eff}})}{1 - \alpha_{\mathrm{v},\lambda} \times S_\lambda(\tau, r_{\mathrm{eff}})}, \tag{4}$$

Cloud reflectance, cloud transmittance, spherical albedo and cloud albedo have all been computed for both water and ice clouds. For radiative transfer simulations with water clouds Mie calculations (Wiscombe, 1980) have been performed beforehand to compute scattering phase functions as well as single scattering albedo and normalized extinction coefficient, which serve as input to MOMO. In the Mie calculations a modified gamma-Hansen cloud droplet size distribution $n(r)$ is assumed (Hansen and Travis, 1974), where the mode radius equals the effective radius (Hansen and Hovenier, 1974):

$$r_{\mathrm{eff}} = \frac{\int_0^\infty r^3 n(r)\mathrm{d}r}{\int_0^\infty r^2 n(r)\mathrm{d}r}, \tag{5}$$

AMTD
7, 4909–4947, 2014

here r is the cloud droplet radius. A typical value of 0.1 for the effective variance is assumed. For ice clouds single-scattering properties described in Baum et al. (2005) have been used in the radiative transfer simulations. Depending on the effective diameter, a mixture of ice habits is assumed based on a number of observations.

From the τ–r_{eff} pair the liquid water path (LWP) for water clouds and the ice water path (IWP) for ice clouds are determined, assuming a plane-parallel homogeneous cloud, as follows:

$$\text{CWP} = \frac{2}{3} \times \tau \times r_{\text{eff}} \times \rho, \tag{6}$$

where ρ is the density of liquid or frozen water (g m^{-3}). For thin ice clouds the following equation is used to compute ice water path, which is based on observations of mid-latitude thin ice clouds (Heymsfield et al., 2003):

$$\text{IWP} = \tau \times \left[\frac{g_0}{r_{\text{eff}}} \times \left[1 + \frac{g_1}{g_0}\right]\right]^{-1}, \tag{7}$$

where g_0 and g_1 are constants with values 0.01256 and 0.725, respectively.

The cloud phase discrimination is done using a simple brightness temperature (BT) threshold of 261 K for the AATSR 10.8 µm channel, combined with a cirrus detection using the brightness temperature difference $\text{BT}_{10.8} - \text{BT}_{12}$ technique (Saunders and Kriebel, 1988) and a maximum reflectance in the visible of 0.25. At 261 K the difference in equilibrium water vapor pressure with respect to ice and water is largest, favoring the growth of ice crystals over super-cooled water droplets for temperatures below 261 K (Pruppacher and Klett, 1997). For the cirrus detection a dynamic clear-sky brightness temperature difference threshold, depending on atmospheric moisture and surface temperature, is used. The clear-sky radiative transfer simulations have been performed with MOMO using a set of standard atmospheric profiles as input taken from McClatchey et al. (1972). From visual inspection of retrieved cloudy scenes the method also often appears to detect cloud edges.

AMTD
7, 4909–4947, 2014

3.2 Cloud top heights

Two cloud top height products are retrieved within FAME-C. First, the cloud top temperature (CTT) using AATSR brightness temperatures is retrieved. Second, the cloud top pressure (CTP) is retrieved using the ratio of the MERIS oxygen-A absorption channel over a nearby window channel. Both cloud top height retrievals are then converted to cloud top heights (in km) using the input atmospheric profiles.

3.2.1 AATSR cloud top temperature

The cloud top temperature is retrieved using measurements at the 11 µm channel and the 12 µm channel, at which the extinction coefficient of water is larger. The forward model, assuming a plane-parallel atmosphere, consists of three parts contributing to the top-of-atmosphere radiation in cloudy situations: cloud, surface, and atmosphere. The contribution of the cloud $I_{c,\lambda}$ is given as follows:

$$I_{c,\lambda} = \epsilon_c(\tau,\theta) \times B(T_{ct},\lambda) \times t_{ct\rightarrow 1,\lambda}(\theta), \quad (8)$$

where ϵ_c is the cloud emissivity, $B(T_c)$ is the Planck function at the temperature of the cloud top T_c, assuming the cloud to be in thermal equilibrium with the surrounding air, and $t_{ct\rightarrow 1}$ is the atmospheric transmittance from the cloud top to the top of atmosphere. The cloud emissivity is computed as follows:

$$\epsilon_c = 1 - \exp\left[\frac{-\tau_{ir}}{\cos\theta}\right], \quad (9)$$

where τ_{ir} is the cloud optical thickness in the infrared. Here, no multiple scattering is assumed and the infrared cloud optical thickness is computed from the visible cloud optical thickness τ_{vis}, which is taken from the cloud micro-physical retrieval. The simple relationship $\tau_{ir} = 0.5 \times \tau_{vis}$ is used, which is about true for large water and ice particles (Minnis et al., 1993).

AMTD
7, 4909–4947, 2014

The contribution of the surface $I_{s,\lambda}$ is given as follows:

$$I_{s,\lambda} = \epsilon_{s,\lambda} \times B(T_s, \lambda) \times t_{a,\lambda}(\theta) \times t_c(\theta), \quad (10)$$

where ϵ_s is the surface emissivity, $B(T_s)$ is the Planck function at the surface temperature T_s, t_a is the transmittance of the atmosphere, and t_c is the transmittance of the cloud. The cloud transmittance is computed from the cloud emissivity with $t_c = 1 - \epsilon_c$. The contribution of the atmosphere at the top of atmosphere $I_{a,\lambda}$ is given as follows:

$$I_{a,\lambda} = \int_{t_{s,\lambda}}^{1} B(T_a, \lambda) \mathrm{d}t_\lambda + [1 - \epsilon_{s,\lambda}] \times t_{s,\lambda}(\theta)^2 \times \int_{t_{s,\lambda}}^{1} \frac{B(T_a, \lambda)}{t_\lambda(\theta)^2} \mathrm{d}t_\lambda, \quad (11)$$

where t_s is the total transmittance from surface to the top of the atmosphere, and $B(T_a)$ is the Planck function at the atmospheric temperature T_a of the level with transmittance t. The second term in the equation is of second order and arises from downward radiance reflected upward at the surface. For cloudy layers, the atmospheric transmittance $t_{a,j}$ of layer j is multiplied by the cloud transmittance $t_{c,j}$ to get the total transmittance t at layer j. The vertical extension of the cloud and the vertical distribution of cloud layer transmittance/emissivity values are based on vertical cloud profiles explained in Sect. 3.2.2. For atmospheric levels below the cloud the atmospheric transmittances are multiplied by the total cloud transmittance t_c. For very thick clouds with cloud emissivities equal to 1, the surface and atmospheric layers below the cloud do not contribute to the top-of-atmosphere radiance.

The fast radiative transfer model RTTOV version 9.3 (METOffice, 2013) is used to simulate the clear-sky transmission for both AATSR IR channels at a given number of atmospheric levels. As input to RTTOV are given atmospheric profiles of temperature, water vapour and ozone concentrations, as well as the temperature, water vapour concentration and pressure near the surface. The atmospheric profiles and surface properties are obtained from a numerical weather prediction model. At the time of development the optical parameter file for ATSR on ERS (version 7) was used. This will

AMTD
7, 4909–4947, 2014

lead to a small error in the simulated AATSR brightness temperatures due to slightly different spectral response functions for the IR channels of the two instrument.

3.2.2 MERIS cloud top pressure

The cloud top pressure (CTP) is retrieved using the radiance ratio of the MERIS oxygen-A absorption channel 11 at around 760 nm (L_{11}) and a near-by window channel 10 at around 753 nm (L_{10}), representing an apparent transmittance:

$$t_{O_2} = \frac{L_{11}}{L_{10}}, \tag{12}$$

Since oxygen is a well-mixed gas in the atmosphere, the ratio can be used to estimate the average photon path length through the atmosphere. In cloudy situations this average photon path length mainly depends on cloud top pressure.

MOMO radiative transfer simulations are performed to create LUTs in which the ratio depends on cloud top pressure as well as cloud optical thickness, viewing geometry, surface pressure, and the MERIS channel 11 center wavelength. A US standard atmosphere (McClatchey et al., 1972) is assumed in the simulations. The *k*-distribution method (Bennartz and Fischer, 2000; Doppler et al., 2014) is used to compute the absorption coefficients of the atmospheric gases. Information on the position and width of absorption lines is taken from the HITRAN database (Rothman et al., 2009). For cloud layers below 440 hPa ice crystals are assumed with a fixed effective radius of 40 µm, otherwise water droplets are assumed with a fixed effective radius of 10 µm. A previous sensitivity study (Preusker and Lindstrot, 2009) has shown that the cloud micro-physical properties and the temperature profile account for errors of less than 10 and 20 hPa, respectively, in the MERIS-CTP retrieval and are much smaller than other error sources. For CTP retrievals above high land surfaces the surface pressure has to be taken into account to prevent underestimation of CTP. For retrievals above oceans a surface pressure of 1013 hPa is assumed. To account for the spectral smile effect in the MERIS measurements (Bourg et al., 2008), which is the variation of the channel

AMTD
7, 4909–4947, 2014

center wavelength along the field-of-view, radiative transfer simulations are performed for varying center wavelengths in the oxygen-A absorption channel. The spectral calibration from Lindstrot et al. (2010) is used to account for this.

Due to in-cloud scattering the average photon path length is increased. This increase depends on the vertical extinction profile of the cloud. To derive "realistic" cloud vertical extinction profiles for nine cloud types based on the ISCCP cloud classification (ISCCP), one year (2010) of layer optical thicknesses as provided by the CloudSat database is used as described in Henken et al. (2013). The resulting averaged and normalized vertical extinction profiles are shown in Fig. 2. It can be seen that for most cloud types lower cloud layers tend to have higher extinction values than upper cloud layers. These vertical extinction profiles have been used in the simulations of the MERIS channel 10 and 11 radiances, selecting the appropriate profile according to the ISCCP cloud classification. The total cloud optical thickness is taken from the cloud micro-physical retrieval.

3.3 Auxiliary data

A set of auxiliary data is needed within the FAME-C algorithm. For the atmospheric correction in the cloud micro-physical retrieval, atmospheric profiles from ERA-Interim re-analzses (00:00 UTC and 12:00 UTC) and forecasts (06:00 UTC and 18:00 UTC) are used. They are linearly interpolated in time, but kept on the ERA-Interim spatial resolution of 1.125°. The interpolated atmospheric profiles and surface properties also serve as input in the RTTOV clear-sky simulations. Furthermore, the IR land surface emissivities are taken from the UW-Madison Baseline Fit Emissivity Database (Seemann et al., 2008). The cloud micro-physical retrieval uses the MODIS 16 day composite white-sky surface albedo product (MCD43C3; NASA Land Processes Distributed Active Archive Center, LP DAAC, 2013) on a 0.05° spatial grid as input, while the MERIS-CTP retrieval uses the 2005 monthly mean MERIS-derived land surface albedo product (Muller et al., 2007). Over the oceans fixed surface albedo and surface emissivity values are taken. To account for pixels that might contain snow-covered surfaces, the MODIS monthly

AMTD
7, 4909–4947, 2014

mean snow cover product (MYD10CM; Hall et al., 2006) on a spatial 0.05° grid is used. Sea ice cover is taken from ERA-Interim. For pixels containing snow or sea ice, the surface albedo and surface emissivity values are adjusted accordingly. The surface pressure that serves as input in the MERIS-CTP retrieval is estimated on a pixel basis from the MERIS surface height provided as meta-data in the AATSR-MERIS synergy product. The synergy product also provides for a pixel-based land–sea mask.

4 Retrieval scheme

The FAME-C cloud property retrieval is conducted orbit-wise on a pixel basis and in a sequential form. First, preprocessing is performed creating the synergy files with cloud mask as well as extracting auxiliary data. Then, for pixels identified as cloudy during the cloud screening, the cloud micro-physical retrieval is performed (DCOMP). Last, the cloud top height retrievals are performed (DCHP; Daytime Cloud top Height Properties). Note, the cloud optical thickness from the micro-physical retrieval serves as input for the cloud top height retrievals. Figure 1 gives a schematic overview of the FAME-C algorithm.

4.1 Inversion technique

The retrieval of the cloud parameters is based on the optimal estimation method. This inversion technique allows for the combined use of an a-priori estimate of the most likely solution, $\boldsymbol{x}_\mathrm{a}$, and the measurements given in the measurement vector $\boldsymbol{y}$, to maximize the probability of the retrieved cloud parameters given in the state vector $\boldsymbol{x}$. Both $\boldsymbol{x}_\mathrm{a}$ and $\boldsymbol{y}$ are weighted by their uncertainty estimates given in the error covariance matrices $\mathbf{S}_\mathrm{a}$ and $\mathbf{S}_y$, respectively. In short, this inversion technique aims to minimize the retrieval cost function J given as:

$$J = [\boldsymbol{y} - F(\boldsymbol{x}, \boldsymbol{b})]^\mathrm{T} \mathbf{S}_y^{-1} [\boldsymbol{y} - F(\boldsymbol{x}, \boldsymbol{b})] + [\boldsymbol{x} - \boldsymbol{x}_\mathrm{a}]^\mathrm{T} \mathbf{S}_\mathrm{a}^{-1} [\boldsymbol{x} - \boldsymbol{x}_\mathrm{a}], \quad (13)$$

AMTD
7, 4909–4947, 2014

where $F(\boldsymbol{x}, \boldsymbol{b})$ is the output of the forward model for state $\boldsymbol{x}$ and background state $\boldsymbol{b}$. The background state vector, or forward model parameter vector, includes parameters that are not retrieved, but do affect the retrieval. Due to non-linearity in the forward model the minimization is performed within an iterative process, whereby a first guess is used to start the iteration and a specified convergence criterion to end the iteration. At the end of the iteration, the error covariance matrix of the retrieved state $\mathbf{S}_x$ can be computed as follows:

$$\mathbf{S}_x = \left[\mathbf{K}_T \mathbf{S}_y^{-1} \mathbf{K} + \mathbf{S}_a^{-1}\right]^{-1}, \quad (14)$$

where $\mathbf{K}$ is the averaging kernel describing the sensitivity of $\boldsymbol{y}$ to changes in state parameters. This way, the pixel-based retrievals are accompanied by pixel-based uncertainties.

It has to be noted that the optimal estimation method is built on the assumption that the state parameters and their errors show a Gaussian distribution and the iteration method assumes that the measurements change linearly with small changes in the state parameters. To meet these assumptions, the $\tau - r_{\text{eff}}$ pair is retrieved in a logarithm-based space. An in-depth mathematical description of optimal estimation can be found in Rodgers (2000).

Figure 3 shows an example of the cloud mask and retrieved cloud parameters for a cloudy scene above Germany.

4.2 Uncertainty estimates

The reliability of the error covariance matrix of the retrieved state depends on the reliability of the characterization of $\mathbf{S}_a$ and $\mathbf{S}_y$, i.e. on the estimated uncertainties in the measurements and the a-priori state. Also, forward model parameter uncertainties, which are uncertainties caused by non-retrieved parameters in the forward model, can be added to the measurement uncertainties to form a combined measurement error

AMTD
7, 4909–4947, 2014

covariance matrix $\mathbf{S}_\epsilon$ as follows:

$$\mathbf{S}_\epsilon = \mathbf{S}_y + \mathbf{K}_B \mathbf{S}_B \mathbf{K}_B^T, \quad (15)$$

where $\mathbf{S}_B$ is the forward model error covariance matrix, and $\mathbf{K}_B$ is the averaging kernel, which describes the sensitivity of $\boldsymbol{y}$ to changes in the forward model parameters.

At the moment all error covariance matrices only have non-zero values for the diagonal elements, meaning that correlations between uncertainties are neglected. Furthermore, we do not make use of an independent source that can provide for a well-characterized a-priori knowledge of the cloud parameters and their uncertainties. Therefore, the estimated uncertainties are set to very high values. This will reduce the constrain of the a-priori estimate $\boldsymbol{x}_a$ on possible solutions $\boldsymbol{x}$, and basically reduces the optimal estimation method to a maximum likelihood method. Estimated uncertainties in the measurements (based on ESA, 2013b, for AATSR) as well as for a set of forward model parameters are listed in Table 2. To account for uncertainties due to the rather simple cloud phase discrimination, the forward model parameter uncertainties of both the water clouds and ice clouds are added to the measurement error covariance for certain pixels. This is done for pixels with 10.8 µm brightness temperatures between 245 K and 273 K and where the reflectance pair 0.6–1.6 µm lies within both the water and ice cloud LUT. Figure 4 shows the atmospheric corrected 0.6 and 1.6 µm reflectances for cloudy pixels from the scene as shown in Fig. 3 together with the AATSR LUT reflectances for a mean viewing geometry and surface albedo, as function of cloud optical thickness and effective radius and for both water and ice clouds. In green are shown the cloudy pixels with an uncertain retrieved cloud phase located in the overlapping area of the water and ice LUT. According to our forward models in this area we can have both large water droplets and small ice crystals or a mix of both.

The retrieved uncertainties for all cloudy pixels, and for each retrieved cloud phase from the scene mentioned above are shown in Fig. 5. For COT, REF and CWP, the mean relative uncertainty is lowest for about 10, 10 µm and 100 g m^{-2}, respectively, and increases for both decreasing and increasing values of the accompanying cloud

AMTD
7, 4909–4947, 2014

properties. For both CTT and CTP the relative uncertainty decreases for decreasing cloud top height. The shapes can be largely explained as follows. For thin clouds the surface albedo uncertainty has a large contribution as well as the uncertainty in cloud emissivity. For very thick clouds the reflectance in the visible is less sensitive to cloud optical thickness leading to an increased uncertainty in COT. The uncertainties in cloud emissivity and COT are propagated to uncertainties in CTT and CTP, respectively. In general, the relative uncertainty is highest for pixels with uncertain cloud phase and lowest for water cloud pixels.

Uncertainties in ERA-Interim atmospheric profiles are neglected. Also, uncertainties in the radiative transfer simulations, chosen cloud micro-physical models, and due to interpolations in the LUTs are not considered at present.

Last, the forward model assumes fully cloudy pixels with plane-parallel clouds either consisting of water droplets or ice crystals. The impact of sub-pixel clouds, 3-dimensional effects (e.g. cloud shadows), multi-layer cloud situations, and mixed-phase clouds, needs to be studied in the future for an improved uncertainty estimate budget.

5 Verification

To verify the performance of the FAME-C cloud properties two comparisons were performed for selected areas and for the years 2007–2009.

5.1 Comparison to MODIS-TERRA level-2 cloud micro-physical properties

The comparison of the FAME-C level-2 cloud micro-physical properties to the MODIS-TERRA level-2 cloud micro-physical properties (MOD06 collection-5 cloud products) is performed for four selected regions as shown in Fig. 6. For each region all available orbit segments of both ENVISAT and TERRA are collected. Overpasses of the satellites TERRA and ENVISAT do not necessarily occur on same days. Therefore, no pixel-based comparison is possible. For all selected cloudy pixels within the region and within

AMTD
7, 4909–4947, 2014

one month, monthly means and standard deviations are produced for each of the cloud micro-physical properties.

For both, only cloudy pixels with satellite viewing angles of < 21.6°, which is the maximum AATSR satellite viewing angle, and solar zenith angles of < 70° are considered. For MODIS-TERRA level-2, the effective radius is limited to 30 µm for water clouds. In this comparison this is also done for FAME-C effective radius for water clouds. Furthermore, for the MODIS cloud micro-physical properties cloudy pixels with a good general assessment according to the quality flag are selected. For FAME-C successfully converged cloudy pixels are selected.

Figure 7 shows the frequency distribution of COT, REF and CWP for all retrieved cloudy pixels in the time period 2007–2009 for both FAME-C and MODIS-TERRA for two selected regions GER and NAM as presented in Fig. 6. Also a distinction in cloud phase is made. Generally, the overall distributions agree well with similar shapes and peaks located around similar values. Especially for NAM this is expected since one cloud regime, marine stratocumulus clouds, dominates this region. Differences become larger when only considering one specific cloud phase. For NAM both FAME-C and MODIS-TERRA agree that almost all pixels consist of the water cloud phase. For both regions, FAME-C has a larger number of pixels with cloud phase uncertain. A major difference is the sharp peak at low COT values for FAME-C, mainly consisting of ice phase. These are misidentified cirrus clouds and the peak vanishes when these pixels are not considered. Consequently, the peak CWP is shifted towards lower values for FAME-C. The MODIS-TERRA REF values agree very well for NAM. In GER, the second peak in the MODIS-TERRA REF arising from the ice cloud phase is not visible in FAME-C REF.

Table 3 lists for each region and cloud property the bias and root mean square error (RMSE) computed from the monthly means in the 3 year period. They have been computed for all cloudy pixels with successful retrieval (All), and separately, for cloudy pixels identified as water cloud (Wat), ice cloud (Ice) and with cloud phase uncertain (Unc). The cloud fraction here is defined as the cloud fraction which only considers

AMTD
7, 4909–4947, 2014

cloudy pixels with a successful retrieval, so those pixels contributing to the statistics of the micro-physical cloud properties. The cloud phase fractions are considered relative to this overall retrieval cloud fraction.

For three regions FAME-C shows an overall cloud fraction that is higher than the MODIS-TERRA overall cloud fraction (positive bias), especially for the regions over the ocean (NAM and SAO). This may partly be explained by the clear-sky restoral in the MODIS-TERRA cloud property retrieval and likely a more strict quality assessment than in FAME-C. The relative water cloud fraction is usually lower for FAME-C, while the uncertain cloud fraction is higher for FAME-C. Generally, the overall tendency is that FAME-C shows lower COTs and higher REFs. Especially noticeable is the COT negative bias for GER. This can be attributed to a large number of optically thin ice clouds retrieved with FAME-C, but not with MODIS-TERRA. First inspections have revealed that this is due to misidentified cirrus clouds, which, through visual inspection, appear to be mainly cloud edges. Neglecting those pixels reduces the overall COT, REF, and REF16 biases to −1.92, 1.01, and 0.45 µm, respectively, but increases the CWP bias to 25.20 g m^{-2}.

The bias between the REF where both FAME-C and MODIS-TERRA retrieved REF using the 1.6 µm channel is not necessarily smaller than the bias when MODIS-TERRA uses the 2.1 µm channel. The NAM region is dominated by marine stratocumulus clouds, which are relatively horizontal homogeneous and sub-adiabatic (e.g., Pawlowska and Brenguier, 2000). An adiabatic cloud shows an increasing REF with height. The penetration depth at 1.6 µm is larger than at 2.1 µm and would result in a lower retrieved effective radius assuming an adiabatic cloud. Therefore, in that case a negative bias would be expected when comparing the FAME-C REF retrieved using 1.6 µm and MODIS-TERRA REF using 2.1 µm. When comparing both REF retrievals at 1.6 µm a slight positive bias is found. Retrievals of REF using different near-infrared channels can however also be affected differently by, e.g., 3-d radiative effects (e.g., Zhang et al., 2012), and makes interpretation of small differences difficult. The CWP bias is largest for the CAF region, this is however also the region where deep

AMTD
7, 4909–4947, 2014

convection takes place which can result in very high CWP values. Mostly, biases are largest for pixels with uncertain cloud phase followed by the ice cloud phase. This is also true for the root mean square error.

It should be noted that the TERRA satellite flies in a sun-synchronous near-polar orbit with a mean local solar time of 10.30 a.m. at descending node, which is half an hour later than the ENVISAT satellite. Slightly shifted observation times as well as different viewing geometry can also contribute to differences in mean cloud properties.

5.2 Comparison to cloud top heights derived from ground-based radar observations

The comparison of FAME-C cloud top height products to cloud top heights derived from ground-based radar observations is performed at ARM sites in the Southern Great Plains and the Tropical Western Pacific. Overpass day and time of the ENVISAT satellite at each site is determined. For each overpass mean and standard deviation of both FAME-C cloud top height products are computed for a 5 by 5 pixel box centred around the pixel that matches best with the ARM site latitude and longitude values. Before doing so, parallax correction was performed for cloudy pixels. Mean and standard deviations were only performed when at least 9 successfully retrieved cloud top heights were present in the 5 by 5 pixel box. The vertical profiles of the radar reflectivity factor and mean doppler velocity from a millimetre cloud radar are used to determine cloud top height and the number of cloud layers. Selected cases are cases where the radar reflectivity factor and mean doppler velocity show at least two adjacent vertical layers with reflectivity factors and mean doppler velocity higher than the pre-defined threshold, which are 30 dBZ and $0\,m\,s^{-1}$, respectively. Cloud top height is defined as the height of the highest valid cloud layer. The mean radar cloud top height is computed from derived radar cloud top heights within one minute of the ENVISAT overpass time. Furthermore, for the comparison only cases with standard deviations of less than 0.5 km for the cloud top heights were selected, resulting in 44 cases for AATSR and 23

AMTD
7, 4909–4947, 2014

for MERIS. This also reflects the fact that at the moment the MERIS cloud top pressure retrieval tends to fail more often than the AATSR cloud top temperature retrieval.

Figure 8 shows the comparison of AATSR and MERIS cloud top heights to radar cloud top heights for single-layer and multi-layer cloud cases. Multi-layer cloud is defined as where the vertical profile of the radar data shows at least five adjacent cloud-free layers (225 m) between cloud layers. In general, the FAME-C cloud top heights are underestimated, except for MERIS cloud top heights for single-layer clouds, where there is an overestimation of cloud top height for mid-level clouds. The absolute bias is largest for multi-layer clouds, but not necessarily the root mean square error. For AATSR cloud top heights for single-layer clouds, large deviations for lower clouds may be attributed to incorrect conversion of cloud top temperature to cloud top height due to temperature inversions. Large deviations for higher clouds occur mainly for optically thin clouds (COT < 5), which suggests the need for an improved cloud property retrieval for cirrus clouds.

6 Summary and discussion

This paper is intended to serve as a reference paper to the FAME-C algorithm, which is used to retrieve daytime cloud micro-physical and macro-physical properties and their uncertainties on a pixel basis. The AATSR and MERIS observations and accompanying forward models are presented as well as the auxiliary data used in FAME-C. As part of the pre-processing AATSR and MERIS observations are collocated and cloud screening is performed using all channels from both instruments. Next, for all cloudy pixels a simple cloud phase detection is performed. The retrieval scheme itself consists of two main steps and is carried out on a pixel-basis for those pixels identified as cloudy by the cloud mask. First, the cloud micro-physical retrieval is performed using an AATSR visible and near-infrared channel, resulting in retrieved cloud optical thickness and effective radius. From those also cloud water path is computed. Separate forward models have been developed for water and ice clouds. Second, the cloud top height retrieval

AMTD
7, 4909–4947, 2014

is performed using observations from AATSR infrared channels for the cloud top temperature retrieval and observations from the MERIS oxygen-A absorption channel for the cloud top pressure retrieval. Especially the MERIS cloud top pressure retrieval depends on the assumed vertical extinction profile of the cloud. Therefore, in both cloud top height retrievals vertically inhomogeneous cloud profiles are assumed derived from one year of CloudSat data. The cloud optical thickness previously retrieved serves as input for both cloud top height retrievals.

The use of the optimal estimation method in the retrieval scheme allows for a propagation of a-priori knowledge and the uncertainty estimates of the measurements and forward model parameters into the final retrieval of the cloud property and its uncertainty. At this point, the contribution of the a-priori estimate in FAME-C to the retrieved state and its uncertainty is negligible. Efforts are shown on the estimation of uncertainties in the measurements and forward model parameters. Both the inclusion of independent a-priori knowledge and a more extended uncertainty estimate budget and assessment are envisaged for in the future to fully exploit the advantages of the optimal estimation method.

A comparison to MODIS-TERRA monthly means derived from level-2 cloud products for four selected regions was performed for cloud fraction, cloud phase, and the cloud micro-physical properties. Results show an overall good agreement between FAME-C and MODIS cloud micro-physical properties. Differences do become larger when looking at biases and root mean square errors for one specific cloud phase. The comparison of the FAME-C cloud top height products and cloud top heights derived from cloud radars reveal an underestimation of FAME-C cloud top height and quite a large root mean square error. The FAME-C retrieved cirrus cloud properties have a large contribution to differences in both comparisons. For in-depth FAME-C cloud top heigh retrieval evaluations, the comparisons will be extended to CloudSat and CALIPSO observations of cloud top heights for scenes where ENVISAT and A-train had overlapping overflights.

AMTD
7, 4909–4947, 2014

Ongoing FAME-C retrieval developments and verifications, taking place within phase 2 of the ESA Climate Change Initiative Cloud project, focus on a more advanced cloud phase retrieval, an improved cirrus cloud detection, and a separate forward model for multi-layer cloud situations. Also, the difference in retrieved cloud top heights from AATSR and MERIS and its relation to cloud vertical extension is one of the main topics of interest. Furthermore, it is planned to adapt FAME-C to retrieve all cloud properties at once resulting in a physically more consistent retrieval. Further ongoing work includes verification efforts on larger spatial scales, comparisons of seasonal and inter-annual variations, and comparisons to other satellite-derived cloud properties as well as cloud properties derived from ground-based observations.

Acknowledgements. The authors would like to thank ESA for providing the funding for this study within the frame of the ESA CCI Cloud project. Also, the authors would like to thank Andi Walther for fruitful discussions and for providing the MODTRAN based AATSR atmospheric absorption coefficients, and Martin Stengel for help with the ERA-Interim data. Furthermore, the authors would also like to thank NASA-LAADS for providing the MODIS-TERRA cloud products and the ARM Program Climate Research Facility for providing cloud radar data.

References

Baum, B. A., Yang, P., Heymsfield, A. J., Platnick, S., King, M. D., Hu, Y., and Bedka, S. T.: Bulk scattering properties for the remote sensing of ice clouds, Part II: Narrowband models, J. Appl. Meteorol., 44, 1896–1911, 2005. 4918

Bennartz, R. and Fischer, J.: A modified *k*-distribution approach applied to narrow band water vapour and oxygen absorption estimates in the near infrared, J. Quant. Spectrosc. Ra., 66, 539–553, 2000. 4921

Bourg, L., D'Alba, L., and Colagrande, P.: MERIS Smile effect characterisation and correction, ESA Technical Note, 2008. 4921

Doppler, L., Preusker, R., Bennartz, R., and Fischer, J.: *k*-bin and *k*-IR: *k*-distribution methods without correlation approximation for non-fixed instrument response function and extension to the thermal infrared-applications to satellite remote sensing, J. Quant. Spectrosc. Ra., 133, 382–395, 2014. 4921

AMTD
7, 4909–4947, 2014

ESA: MERIS Quality Working Group: MERIS 3rd data reprocessing, Software and ADF updates, Tech. Rep. A879.N T.008.ACRI-ST, ACRI, Technical report, ESA, available at: http://earth.eo.esa.int/pcs/envisat/meris/documentation/ (last access: May 2014), 2011. 4914

ESA: BEAM Earth Observation Toolbox and Development Platform, online, available at: http://www.brockmann-consult.de/cms/web/beam (last access: May 2014), 2013a. 4914

ESA: AATSR Handbook, section "Pre-flight characteristics and expected performance", online, available at: https://earth.esa.int/handbooks/aatsr/CNTR3-2-1.htm (last access: May 2014), 2013b. 4925

ESA: ESA Cloud CCI, online, available at: www.esa-cloud-cci.org (last access: May 2014), 2013c. 4912

ESA: ESA Earthnet Online: ENVISAT Mission, online, available at: http://earth.esa.int/web/guest/missions/esa-operational-eo-misions/envisat (last access: May 2014), 2013d. 4914

ESA: SENTINEL-3, online, available at: http://www.esa.int/Our_Activities/Observing_the_Earth/Copernicus/Sentinel-3 (last access: May 2014), 2013e. 4913

Fell, F. and Fischer, J.: Numerical simulation of the light field in the atmosphere–ocean system using the matrix-operator method, J. Quant. Spectrosc. Ra., 69, 351–388, 2001. 4915

Gómez-Chova, L., Camps-Valls, G., Munoz-Marı, J., Calpe, J., and Moreno, J.: Cloud screening methodology for MERIS/AATSR Synergy products, in: Proc. 2nd MERIS/AATSR User Workshop', ESRIN, Frascati, 22–26, 2008. 4914

Gómez-Chova, L., Camps-Valls, G., Calpe, J., Munoz, J., and Moreno, J.: Cloud Screening ATBD, Algorithm theoretical basis document, University of Valencia, 2010. 4914

Hall, D. K., Salomonson, V. V., and Riggs., G. A.: MODIS/Aqua Snow Cover Monthly L3 Global 0.05Deg CMG, Version 5. [2007–2009], online, available at: http://nsidc.org/data/myd10cm.html (last access: May 2014), 2006. 4923

Hansen, J. E. and Hovenier, J.: Interpretation of the polarization of Venus, J. Atmos. Sci, 31, 1137–1160, 1974. 4917

Hansen, J. E. and Travis, L. D.: Light scattering in planetary atmospheres, Space Sci. Rev., 16, 527–610, 1974. 4917

Henken, C. C., Lindstrot, R., Filipitsch, F., Walther, A., Preusker, R., and Fischer, J.: FAME-C: Retrieval of cloud top pressure with vertically inhomogeneous cloud profiles, in: AIP Conference Proceedings, Vol. 1531, 412 pp., 2013. 4922

Heymsfield, A. J., Matrosov, S., and Baum, B.: Ice water path-optical depth relationships for cirrus and deep stratiform ice cloud layers, J. Appl. Meteorol., 42, 1369–1390, 2003. 4918

AMTD
7, 4909–4947, 2014

Hollstein, A. and Fischer, J.: Radiative transfer solutions for coupled atmosphere ocean systems using the matrix operator technique, J. Quant. Spectrosc. Ra., 113, 536–548, 2012. 4915

IPCC: IPCC, 2013: Summary for policymakers, in: Climate Change 2013: The Physical Science Basis, Tech. rep., 2013. 4911

ISCCP: International Satellite Cloud Climatology Project, online, available at: http://isccp.giss.nasa.gov/ (last access: May 2014), 2013. 4911

Lindstrot, R., Preusker, R., and Fischer, J.: Empirical correction of stray light within the MERIS oxygen A-band channel, J. Atmos. Ocean. Tech., 27, 1185–1194, 2010. 4915, 4922

McClatchey, R. A., Fenn, R., Selby, J. A., Volz, F., and Garing, J.: Optical properties of the atmosphere, Tech. rep., DTIC Document, 1972. 4918, 4921

METOffice: RTTOV v9, online, available at: http://research.metoffice.gov.uk/research/interproj/nwpsaf/rtm/rtm_rttov9.html (last access: May 2014), 2013. 4920

Minnis, P., Liou, K.-N., and Takano, Y.: Inference of cirrus cloud properties using satellite-observed visible and infrared radiances, Part I: Parameterization of radiance fields, J. Atmos. Sci., 50, 1279–1304, 1993. 4919

Minnis, P., Szedung, S.-M., Young, D. F., Heck, P. W., Garber, D. P., Chen, Y., Spangenberg, D. A., Arduini, R. F., Trepte, Q. Z., Smith, W. L., Ayers, J. K., Gibson, S. C., Miller, W. F., Hong, G., Chakrapani, V., Takano, Y., Liou, K.-N., Yu, X., and Yang, P.: CERES edition-2 cloud property retrievals using TRMM VIRS and Terra and Aqua MODIS data – Part I: Algorithms, IEEE T. Geosci. Remote, 49, 4374–4400, 2011. 4912

Muller, J.-P., Preusker, R., Fischer, J., Zuhlke, M., Brockmann, C., and Regner, P.: ALBEDOMAP: MERIS land surface albedo retrieval using data fusion with MODIS BRDF and its validation using contemporaneous EO and in situ data products, in: Geoscience and Remote Sensing Symposium, 2007, IGARSS 2007, IEEE International, 2404–2407, 2007. 4922

Nakajima, T. and King, M. D.: Determination of the optical thickness and effective particle radius of clouds from reflected solar radiation measurements, Part I: Theory, J. Atmos. Sci., 47, 1878–1893, 1990. 4915

Nakajima, T. Y. and Nakajma, T.: Wide-area determination of cloud microphysical properties from NOAA AVHRR measurements for FIRE and ASTEX regions, J. Atmos. Sci., 52, 4043–4059, 1995. 4915

NASA: MODIS CERES Science Team, online, available at: http://ceres.larc.nasa.gov/ (last access: May 2014), 2013a. 4911

AMTD
7, 4909–4947, 2014

NASA: MODIS Science Team, Atmosphere, Cloud, online, available at: http://modis-atmos.gsfc.nasa.gov/MOD06_L2/index.html (last access: May 2014), 2013b. 4911
NASA Land Processes Distributed Active Archive Center (LP DAAC), Sioux Falls, S. D. U.: MODIS/Terra+Aqua Albedo 16-Day L3 Global 0.05Deg CMG, Version 5. [2007–2009], online, available at: https://lpdaac.usgs.gov/ (last access: May 2014), 2013. 4922
PATMOS-X: PATMOS-X, online, available at: http://cimss.ssec.wisc.edu/patmosx/overview.html, (last access: May 2014), 2013. 4911
Pawlowska, H. and Brenguier, J.-L.: Microphysical properties of stratocumulus clouds during ACE-2, Tellus B, 52, 868–887, 2000. 4928
Poulsen, C. A., Siddans, R., Thomas, G. E., Sayer, A. M., Grainger, R. G., Campmany, E., Dean, S. M., Arnold, C., and Watts, P. D.: Cloud retrievals from satellite data using optimal estimation: evaluation and application to ATSR, Atmos. Meas. Tech., 5, 1889–1910, doi:10.5194/amt-5-1889-2012, 2012. 4912
Preusker, R. and Lindstrot, R.: Remote sensing of cloud-top pressure using moderately resolved measurements within the oxygen a band-A sensitivity study, J. Appl. Meteorol. Clim., 48, 1562–1574, 2009. 4921
Pruppacher, H. R. and Klett, J. D.: Microphysics of Clouds and Precipitation, 2nd Edn., Kluwer Academic Publishers, 1997. 4918
Rodgers, C. D.: Inverse methods for atmospheric sounding: Theory and Practice, Series on Atmospheric, Oceanic and Planetary Physics, Vol. 2, 2000. 4924
Roebeling, R., Feijt, A., and Stammes, P.: Cloud property retrievals for climate monitoring: Implications of differences between Spinning Enhanced Visible and Infrared Imager (SEVIRI) on METEOSAT-8 and Advanced Very High Resolution Radiometer (AVHRR) on NOAA-17, J. Geophys. Res.-Atmos., 111, 20210, doi:10.1029/2005JD006990, 2006. 4912, 4915
Roebeling, R., Baum, B., Bennartz, R., Hamann, U., Heidinger, A., Thoss, A., and Walther, A.: Evaluating and improving cloud parameter retrievals, B. Am. Meteorol. Soc., 94, ES41–ES44, 2013. 4912
Rothman, L. S., Gordon, I. E., Barbe, A., Benner, D. C., Bernath, P. F., Birk, M., Boudon, V., Brown, L. R., Campargue, A., Champion, J.-P., Chance, K., Coudert, L. H., Dana, V., Devi, V. M., Fally, S., Flaud, J.-M., Gamache, R. R., Goldman, A., Jacquemart, D., Kleiner, I., Lacome, N., Lafferty, W. J., Mandin, J.-Y., Massie, S. T., Mikhailenko, S. N., Miller, C. E., Moazzen-Ahmadi, N., Naumenko, O. V., Nikitin, A. V., Orphal, J., Perevalov, V. I., Perrin, A., Predoi-Cross, A., Rinsland, C. P., Rotger, M., Šimečková, M., Smith, M. A. H., Sung,

AMTD
7, 4909–4947, 2014

K., Tashkun, S. A., Tennyson, J., Toth, R. A., Vandaele, A. C., and Vander Auwera, J.: The HITRAN 2008 molecular spectroscopic database, J. Quant. Spectrosc. Ra., 110, 533–572, 2009. 4921

Saunders, R. and Kriebel, K.: An improved method for detecting clear sky and cloudy radiances from AVHRR data, Int. J. Remote Sens., 9, 123–150, 1988. 4918

Seemann, S. W., Borbas, E. E., Knuteson, R. O., Stephenson, G. R., and Huang, H.-L.: Development of a global infrared land surface emissivity database for application to clear sky sounding retrievals from multispectral satellite radiance measurements, J. Appl. Meteorol. Clim., 47, 108–123, 2008. 4922

Smith, D., Poulsen, C., and Latter, B.: Calibration status of the AATSR reflectance channels, in: Proceedings of the MERIS/AATSR Workshop, 2008. 4914

Stubenrauch, C., Rossow, W., Kinne, S., Ackerman, S., Cesana, G., Chepfer, H., and Di, L.: Assessment of Global Cloud Datasets from Satellites, A Project of the World Climate Research Programme Global Energy and Water Cycle Experiment (GEWEX) Radiation Panel, 2012. 4911

Walther, A. and Heidinger, A. K.: Implementation of the daytime cloud optical and microphysical properties algorithm (DCOMP) in PATMOS-x, J. Appl. Meteorol. Clim., 51, 1371–1390, 2012. 4912, 4915, 4917

Wang, M. and King, M. D.: Correction of Rayleigh scattering effects in cloud optical thickness retrievals, J. Geophys. Res., 102, 25915–25926, 1997. 4916

Wiscombe, W. J.: Improved Mie scattering algorithms, Appl. Optics, 19, 1505–1509, 1980. 4917

Zhang, Z., Ackerman, A. S., Feingold, G., Platnick, S., Pincus, R., and Xue, H.: Effects of cloud horizontal inhomogeneity and drizzle on remote sensing of cloud droplet effective radius: case studies based on large-eddy simulations, J. Geophys. Res., 117, D19208, doi:10.1029/2012JD017655, 2012. 4928

AMTD
7, 4909–4947, 2014

Table 1. Atmospheric correction coefficients for AATSR 0.6 µm and 1.6 µm Channels.

	a_0	a_1	a_2
0.6 H_2O	7.86×10^{-5}	3.9971×10^{-3}	-1.06×10^{-4}
0.6 O_3	2.2229×10^{-3}	3.9840×10^{-5}	3.9945×10^{-8}
1.6 H_2O	-2.13×10^{-5}	9.472×10^{-4}	-4.0×10^{-6}

AMTD
7, 4909–4947, 2014

Table 2. Uncertainty estimates of measurements $\boldsymbol{y}$ (R = reflectance, BT = brightness temperature, L=radiance) and forward model parameters in $\boldsymbol{b}$: albedo α, cloud top pressure (CTP), cloud optical thickness (COT), and cloud emissivity ϵ_c. The cloud optical thickness uncertainty $\mathrm{COT}_{\mathrm{unc}}$ is taken from the cloud micro-physical retrieval results. Misc stands for miscellaneous and is an estimated forward model parameter uncertainty arising from differences in spectral response function of ATSR-2 (assumed in cleark-sky RTTOV simulations) and AATSR, and tabular integration.

		$\boldsymbol{y}$	$\boldsymbol{b}$
AATSR COT/REF	R 0.6 µm R 1.6 µm	4 % 4 %	α: 0.02 and CTP: 20 hPa
AATSR-CTT	BT 11 µm BT 12 µm	0.1 K 0.1 K	$\epsilon_c : \tau_{\mathrm{unc}}/2\cos(\theta) \times \exp(-\tau/2\cos(\theta))$ and Misc: 0.5 K
MERIS-CTP	$L_{761\,\mathrm{nm}}/L_{753\,\mathrm{nm}}$	0.004 %	α: 0.02 and COT: $\mathrm{COT}_{\mathrm{unc}}$

AMTD
7, 4909–4947, 2014

Table 3. Results of the comparison with monthly mean MODIS-TERRA cloud micro-phsyical properties for 4 regions as presented in Fig. 6.

		Bias				RMSE			
		All	Wat	Ice	Unc	All	Wat	Ice	Unc
CAF	CF [%]	−1.87	−10.13	−1.95	21.83	12.45	16.24	6.73	22.87
	COT [1]	−1.54	0.58	−3.73	−2.70	4.84	2.08	7.40	7.52
	REF [µm]	0.07	−1.49	0.92	0.28	3.48	1.95	4.10	2.45
	REF16 [µm]	−1.06	−3.11	0.42	0.21	3.56	3.33	4.13	2.03
	CWP [$g\,m^{-2}$]	21.62	4.61	29.05	2.48	83.70	19.11	111.78	75.29
GER	CF [%]	4.70	−11.97	−2.39	29.81	15.59	17.26	9.66	33.82
	COT [1]	−4.57	−3.02	−9.70	−3.03	6.20	5.80	11.91	11.18
	REF [µm]	2.26	0.09	4.50	0.43	3.14	1.38	5.61	3.61
	REF16 [µm]	1.64	−1.01	4.18	1.10	2.78	1.90	5.83	3.04
	CWP [$g\,m^{-2}$]	0.45	−8.39	−40.89	11.31	40.39	35.27	107.55	86.28
NAM	CF [%]	7.57	−2.41	0.08	0.28	12.98	6.08	0.48	2.22
	COT [1]	−0.60	−0.28	−4.94	7.95	1.38	1.27	7.06	10.52
	REF [µm]	−0.31	−0.47	1.59	3.68	1.33	1.34	5.48	5.29
	REF16 [µm]	0.65	0.41	3.60	4.71	1.35	1.18	6.45	6.21
	CWP [$g\,m^{-2}$]	−1.95	−0.18	−27.91	115.42	13.62	14.46	47.44	141.66
SAO	CF [%]	14.23	−1.77	0.26	1.25	16.17	8.30	1.17	2.51
	COT [1]	−1.10	−0.56	−3.57	1.96	1.75	1.43	4.38	5.31
	REF [µm]	1.11	1.11	−1.44	4.38	2.41	2.18	7.04	6.58
	REF16 [µm]	2.00	1.80	2.05	5.38	2.70	2.39	6.92	7.18
	CWP [$g\,m^{-2}$]	−0.28	5.20	−28.78	66.98	17.25	17.16	44.56	88.68

AMTD
7, 4909–4947, 2014

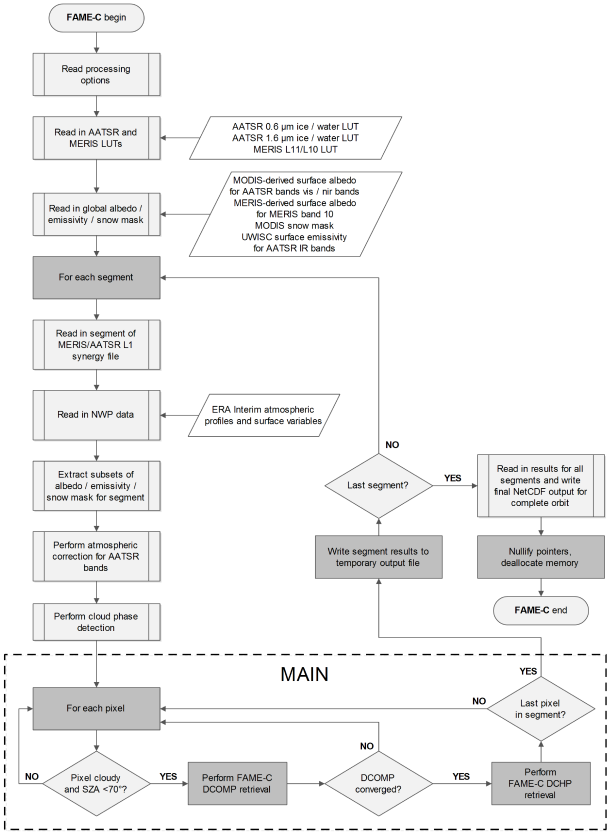

Figure 1. FAME-C algorithm flowchart with two main retrieval steps DCOMP (Daytime Cloud Optical and Microphysical Properties) and DCHP (Daytime Cloud top Height Properties) and input and output data.

AMTD
7, 4909–4947, 2014

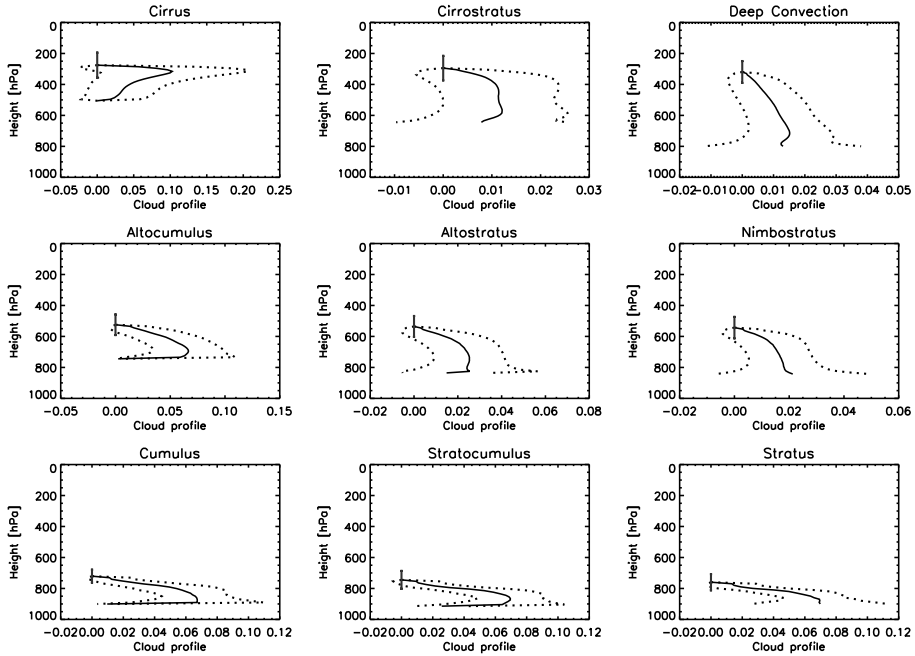

Figure 2. Normalized mean cloud vertical extinction profiles (solid line) for nine cloud types based on the ISCPP cloud classification. Standard deviation of extinction given by the dotted line, and standard deviation of the cloud top pressure given by the error bar.

AMTD
7, 4909–4947, 2014

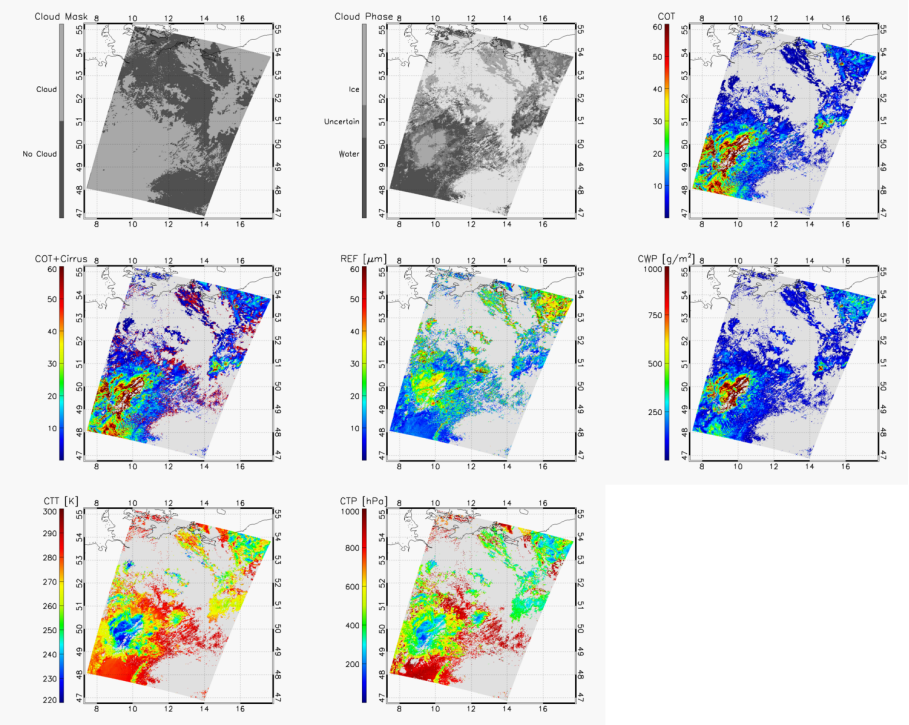

Figure 3. Example of FAME-C cloud mask and retrieved cloud micro-physical and macro-physical properties for a synergy AATSR-MERIS orbit segment above Germany on 21 July 2007.

AMTD
7, 4909–4947, 2014

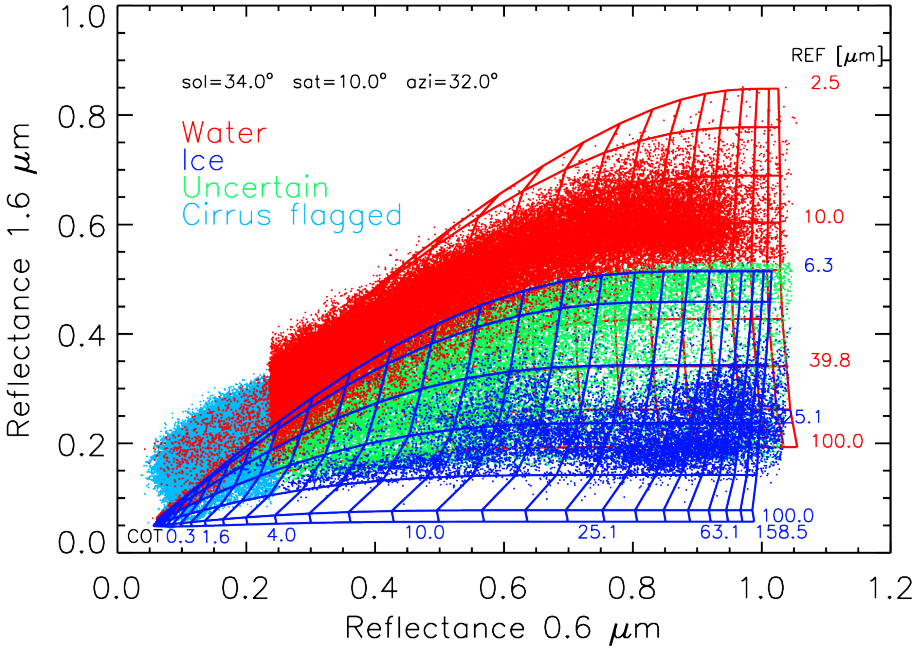

Figure 4. AATSR atmospheric corrected reflectance in visible and near-infrared (dots) for water/ice/uncertain/cirrus pixels from the scene shown in Fig. 3. The two grids represent the forward modelled AATSR reflectances for water (red) and ice (blue) clouds, assuming mean viewing geometry and surface albedo values for the scene.

AMTD
7, 4909–4947, 2014

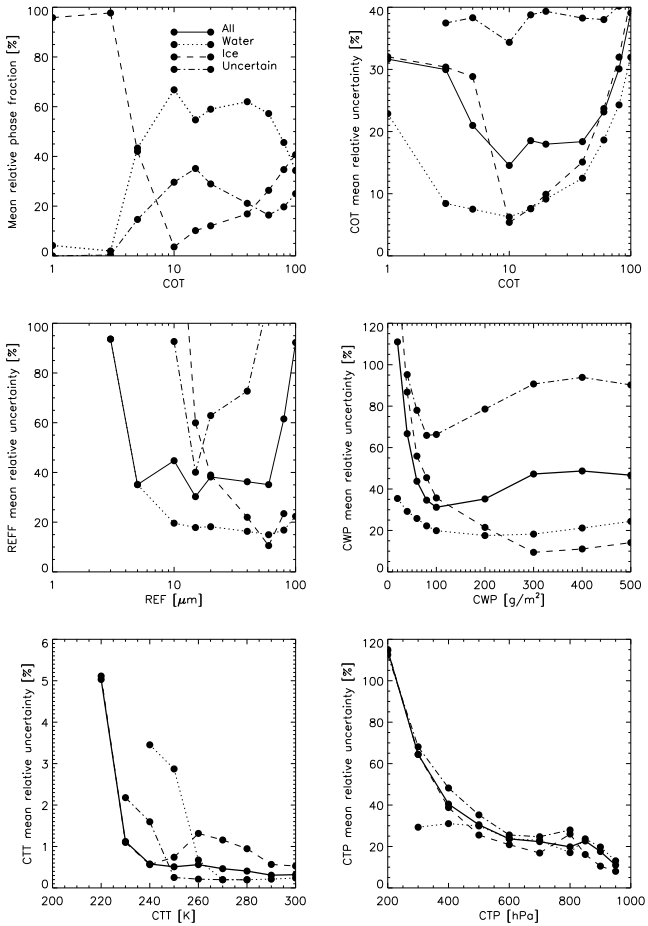

Figure 5. Histograms of mean relative uncertainty estimates for FAME-C cloud properties for all retrieved cloudy pixels for the GER region as presented in Fig. 3.

AMTD
7, 4909–4947, 2014

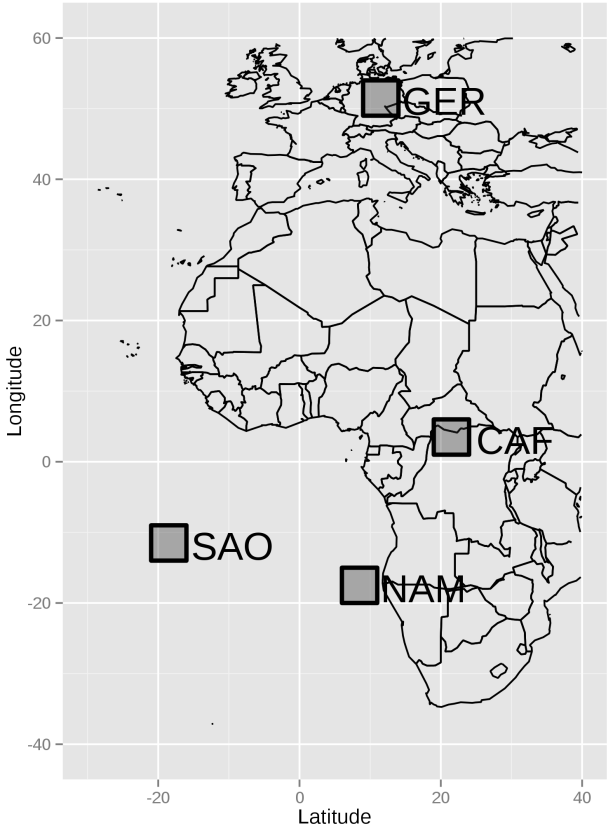

Figure 6. Map showing four regions where Level-2 based comparisons between FAME-C and MODIS-TERRA cloud properties are conducted for the years 2007–2009. SAO = Southern Atlantic Ocean, NAM = Coast of Namibia, CAF = Central Africa, GER = Germany.

AMTD
7, 4909–4947, 2014

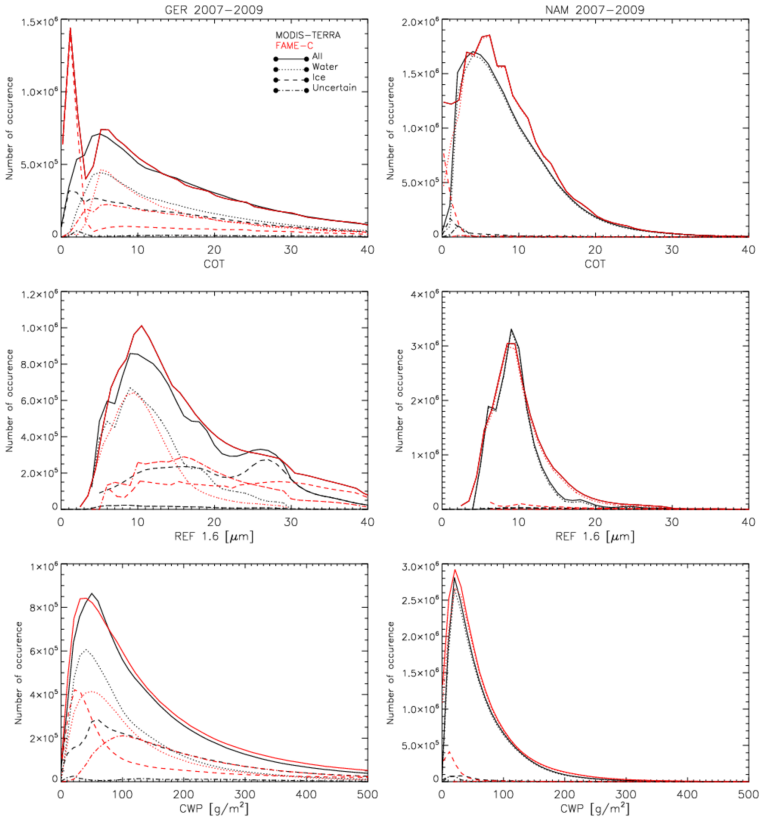

Figure 7. Frequency histograms of the pixel-based retrieved cloud micro-physical properties of FAME-C and MODIS-TERRA for the GER and NAM regions as presented in Fig. 6.

AMTD
7, 4909–4947, 2014

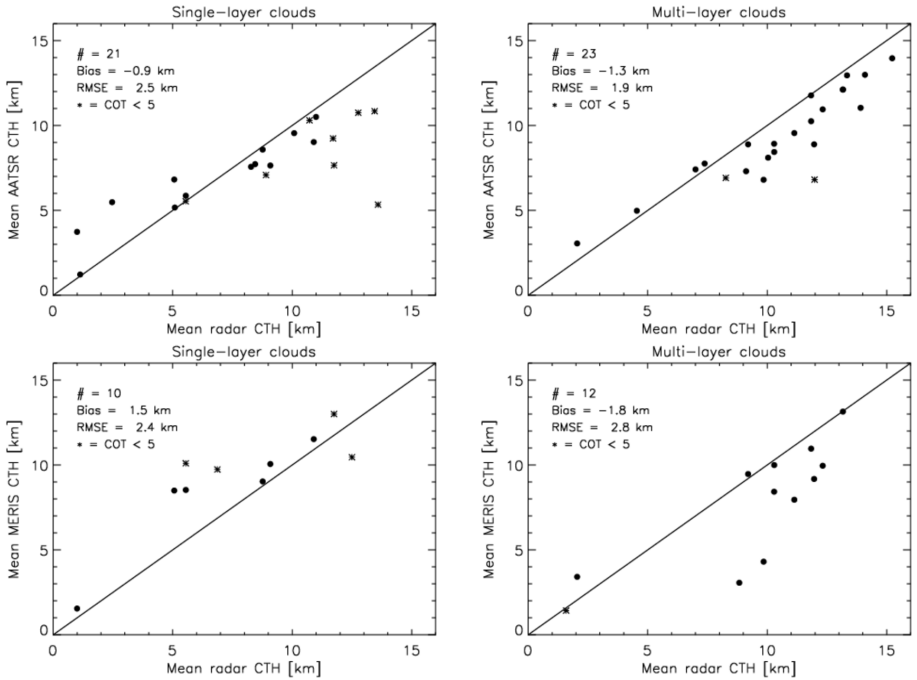

Figure 8. Results of the comparison of AATSR and MERIS mean cloud top height products with mean cloud top heights derived from radar observations at ARM sites. For FAME-C the mean was computed from a 5 by 5 pixel box, for radar the mean was computed from all selected observations within one minute of the ENVISAT overpass time at the site.

AMTD
7, 4909–4947, 2014